18

Nano-Scale Measurements of Dopants in Individual Silicon Nanowires using Kelvin Probe Force Microscopy

Elad Koren[1], Jonathan E. Allen[2], Uri Givan[2], Noel Berkovitch[1], Eric R. Hemesath[2], Lincoln J. Lauhon[2] and Yossi Rosenwaks[1]
[1]*School of Electrical Engineering, Tel-Aviv University,*
[2]*Dept. of Materials Science and Engineering, Northwestern university,*
[1]*Israel*
[2]*USA*

1. Introduction

Semiconductor nanowires are one of the most promising building blocks for near future nano-electronics because they provide a new route to continuing miniaturization as well as a wealth of opportunities in nanoscale science and technology. As the synthesis of new compositionally and morphologically diverse nanowires expands, and the expectations for reliable nanowire devices increase, challenges in nanoscale metrology assume increasing importance. The chemical composition of an individual semiconductor nanowire is of great importance to nanowire electronic properties and device performance, but it is not easy to determine. At least three major challenges in nanowire synthesis and device fabrication are intimately related to the challenge of analyzing nanowire composition: (1) controlling the concentration of intentional dopants; (2) identifying unintentional doping; and (3) electrical junction formation. There are many nanowire systems in which the majority carrier type is controlled by intentional doping (Haraguchi, Katsuyama et al. 1992), but in all cases the actual dopant concentration, its spatial distribution, and the fraction of active dopants are unclear. The origins of dopant compensation (Wang, Lew et al. 2005), including the presence of residual catalyst atoms in nanowires grown by the vapor-liquid-solid (VLS) method (Wagner and Ellis 1964), are therefore speculative. In some material systems, and particularly in quantum dots (Erwin, Zu et al. 2005), impurity doping is known to be difficult. This challenge is compounded by a lack of appropriate characterization tools, and issues such as dopant segregation are generally addressed by indirect means.

Individual nanowires have already been configured as field-effect transistors (Cui and Lieber 2001), photodetectors (Wang, Gudiksen et al. 2001), and bio/chemical sensors (Patolsky, Zheng et al. 2006). The continued advances of these nanometer-scale devices depend critically on knowledge of their atomic-scale structures (Castell, Muller et al. 2003), as compositional fluctuations as small as a single dopant atom can affect a device's performance. Additionally, the important challenge of doping atoms into the 'bulk' of nanowires and nanocrystals, while avoiding surface segregation, further emphasizes the need for 3D composition characterization

of these nanostructures. It should be also emphasized that the performance of almost all current transistor technology depends critically on controlling the concentration and location of dopants to create abrupt homojunctions in Si. Such junctions have been realized in Si nanowires synthesized using the VLS growth mechanism by *in situ* doping, (Gudiksen, Lauhon et al. 2002; Yang, Barrelet et al. 2006) but unintentional surface doping caused by vapor-solid (VS) deposition on the sides of the nanowires (Tutuc, Chu et al. 2006) during growth can complicate the formation of strictly axial homojunctions. Surface doping has been seen in phosphorous-doped Ge nanowires by electrical characterization (Tutuc, Chu et al. 2006) and atom probe tomography, (Perea, Wijaya et al. 2008; Perea, Hernesath et al. 2009) and in doped Si nanowires by Raman spectroscopy (Imamura, Kawashima et al. 2008) and scanning photocurrent microscopy (Allen, Perea et al. 2009). Surface doping and other inhomogeneities are of utmost importance because the success or failure of an integrated circuit is rapidly approaching the point at which a few misplaced atoms can ruin a device. It is highly desirable to determine the atomic scale composition and dopant distribution of individual nanowires with precision, and this is the main objective of this research. As will be show in this review, of our recent work (Koren et al. 2009, 2010, 2011), this can be accomplished by employing combined current-voltage and Kelvin probe force microscopy (KPFM) measurements.

In particular, it shows that KPFM can be use for both longitudinal and radial dopant distribution profiling for *n*-type Si nanowires, grown by the VLS method. The presented results show, that along with a longitudinal non-uniformity, there is also an exponential decrease in dopant concentration across the nanowire radius with a difference of ~ 2 orders of magnitude between the nanowire surface and its core. In addition, the radial dopant profile is consistent with a diffusion coefficient of D~1x10^{-19} m^{2}s^{-1}. This relatively unexpected high diffusivity will be discussed further in this chapter. In addition, low temperature annealing treatment (460 ^{o}C) was used to achieve a uniform dopant distribution. The low temperature treatment was essential to prevent the diffusion of the Au catalyst into the nanowire, which might affect the opto-electronic properties of the Si (Grimmeiss 1977; Queisser 1978).

2. Experimental

2.1 Device fabrication

For all electrical measurements conducted in this chapter, electrical contacts were fabricated through a series of lithography steps. In chronological order, the process for nanowire device fabrication was as follows. First, heavily doped Si (100) substrates with a thin dielectric layer of 200 nm Si_3N_4 were patterned with both large electrodes and a grid used for nanowire location via photolithography and subsequent metal evaporation. Figure 1 presents a typical photolithography pattern for substrate preparation. The metal deposition for the patterned grid and large electrodes consisted of 5 nm of Cr followed by 80 nm of Au. Nanowires were suspended in isopropyl-alcohol solution by low-power sonication of the growth substrate. The nanowires in solution were then drop-cast on the prepared substrates and imaged using an optical microscope. The images were used to establish the position of the nanowires with respect to the patterned grid in the middle of the large contacts so that a high accuracy mask could be designed for electrodes. Then, small electrodes were design by CAD software and written by electron beam lithography (EBL). The electron beam resist

was poly-methyl-methacrylate (PMMA), which was deposited by standard spin coating technique. After developing the EBL pattern, a wet chemical etch with a buffer HF solution was used to remove the native oxide from the nanowires surface, while the residual polymer resist was removed using a standard plasma clean step. Ohmic contacts were fabricated by evaporating Ni immediately after etching.

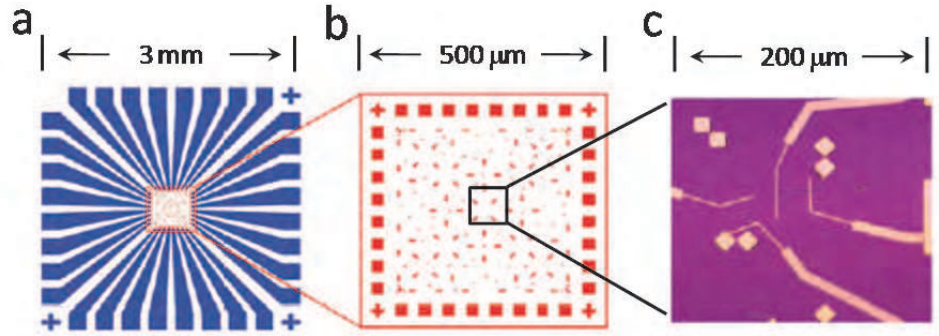

Fig. 1. **(a)** Photolithography pattern for typical device substrate. **(b)** Patterned grid for nanowire location and contacts writing. **(c)** Complete devices after EBL. Taken from (Allen 2008).

2.1.1 Nanowire growth

The Si nanowires used in this study (data summarized in table 1) were grown in a custom-built chemical vapor-deposition reactor designed to provide a large dynamic range in the process variables that most influence nanowire morphology and composition. Silane (SiH_4) has been used as reactant and dilute phosphine (PH_3) has been used as dopant. The background gas composition can be tuned continuously from pure Ar, N_2 and H_2. The ratio of Si to P (in the gas phase) can be varied from 10^6:1 to 10^2:1. Using commercially available colloidal Au nanoparticles, nanowire diameters from 5-100 nm can be grown, and the length is controlled by the growth time. The exact nanowire growth conditions in each part are summarized in the following table:

Part	Au (nm)	Gas phase Dopant:Si	T (°C)	P (Torr)	Carrier gas	Flow rates (SCCM) Carrier/dopant/SiH_4	Time (min)
3	50	1:1500	460	40	N_2	43.3/6.67/2	15
3, 4	50	1:500	460	40	N_2	30/20/2	15
5	80	1:500	460	40	N_2	30/20/2	15

Table 1**.** Growth conditions for the nanowires used in each part.

2.2 Kelvin probe force microscopy

KPFM measures contact potential difference (defined below) at the nanoscale. It is based on the conventional atomic force microscope (AFM) invented in 1985 (Binnig, Quate et al. 1986). KPFM was used for the first time (Martin, Abraham et al. 1988);(Weaver and

Abraham 1991) to measure charges and potential variation on metal surfaces. In this section the basic setup of the KPFM used for our measurements is described.

KPFM measures the contact potential difference (CPD) between a probing tip and a sample. The CPD represents the difference between the tip work-function (ϕ_t) and sample work-function (ϕ_s) and is defined as:

$$CPD = -\frac{1}{q}(\phi_t - \phi_s) \tag{1}$$

The sample work function is a sum of the intrinsic work function and any additional surface potential, thus measuring CPD across a sample surface gives local changes in the surface potential. The basic principle of the measurement is schematically described for a metallic tip and sample in Fig. 2. When the tip and the sample are not connected their Local-vacuum-levels (LVLs) are aligned, but there is a difference in their Fermi levels. Upon electrical connection, electrons flow from the material with the lower work function to the one with a higher work function (in this case from the sample to the tip) as shown in Fig. 2 (b). This process continues until the Fermi levels are aligned; the two materials are now charged and there is a difference in their LVLs. Due to the charging of the tip and the sample, an electrostatic force develops. This force can be nullified by applying an additional bias between the tip and the sample.

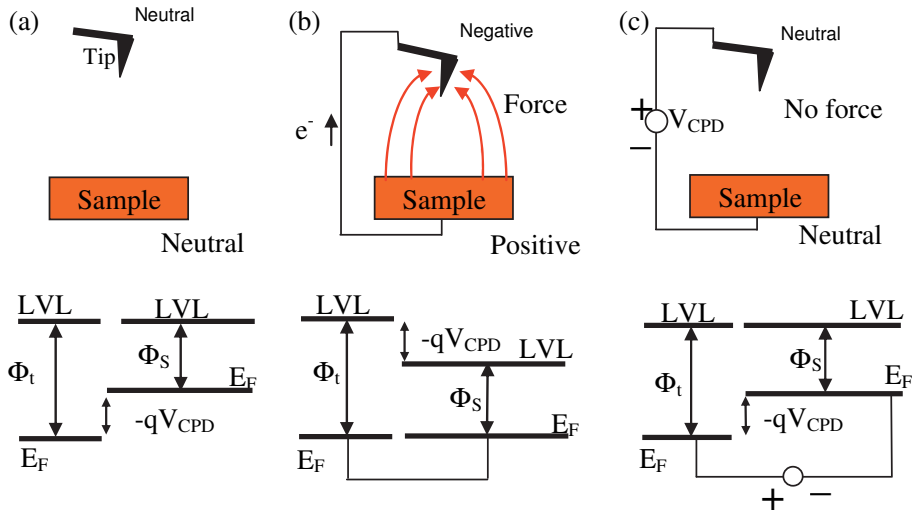

Fig. 2. Basic measurement setup of contact potential difference (CPD).

The magnitude of this bias is the CPD as seen in Fig. 2 (c). The nullifying procedure is based on applying a bias either to the tip or to the sample. The CPD measurement is conducted either in non-contact, or lift modes of the AFM. It is well known that in these modes the forces between the tip and the sample are relatively small, thus modulation (AC) techniques are used in order to increase the force sensitivity. A typical AC measurement is conducted in the following way. An AC bias at a frequency ω is applied between the tip and the

sample. It can be shown (Martin, Abraham et al. 1988) that the force component at this frequency is proportional to the CPD and therefore, can be nullified using a feedback loop whose input is the ω component of the force. The most naive way to derive this force is to treat the tip-sample system as a parallel plate capacitor with one plate as the tip apex, and the other as the sample underneath it (Weaver and Abraham 1991). Under this assumption the force which is just the derivative of the electrostatic energy with respect to the tip-sample separation (z), is given by:

$$F = -\frac{\partial U}{\partial z}\bigg|_Q = -\frac{1}{2}V^2\frac{\partial C}{\partial z} \propto -\frac{1}{2}\frac{V^2}{z^2} \tag{2}$$

where the electrostatic energy (U) is given for a parallel plate capacitor configuration by:

$$U = \tfrac{1}{2}CV^2 \tag{3}$$

with C the tip sample capacitance, and V the potential difference between the AFM tip and the sample. Using the following expression for the potential difference:

$$V = CPD - V_{DC} + V_{AC}\sin(\omega \cdot t) \tag{4}$$

and inserting it in Eq. 2 gives:

$$F \propto \frac{1}{2z^2}\left[(CPD - V_{DC})^2 + (CPD - V_{DC})V_{AC}\sin(\omega \cdot t) + V_{AC}^2\sin(\omega \cdot t)^2\right] \tag{5}$$

Thus the force at frequency ω is indeed proportional to the CPD.
In this work, KPFM measurements were conducted in Lift mode by a commercial AFM system (Dimension 3100 *Veeco, Inc.*). On the first pass, topography is measured in standard Tapping mode. For imaging, the probing tip is driven by a piezoelectric element at a frequency slightly below its first resonance. On the second pass, the mechanical drive to the piezo is turned off, and an alternating voltage, $V_{AC}\ sin(\omega t)$ at the resonance frequency is applied to the cantilever in order to induce an electrostatic force between the tip and the sample. The force at the frequency ω is given by:

$$F_\omega \propto \frac{\partial C}{\partial Z}\left[(V_{CPD} - V_{DC})V_{AC}\sin(\omega \cdot t)\right] \tag{6}$$

Hence the CPD between the tip and the sample surface is measured by nullifying the output signal of a lock-in amplifier, which measures the electrostatic force at the frequency ω.

2.3 Measurements setup

The measurements are conducted in a controlled nitrogen environment glove box (less than ~2 ppm H_2O). Voltages and currents are supplied and measured using Agilent 4155c SPA and a lock in amplifier which are connected to the sample through BNC cables. The samples were placed on a ceramic chip carrier and a wire bonder was used to connect the chip's Gate/Source/Drain contacts to the chip carrier's contacts. The ceramic chip carrier was placed in a chip socket which in turn is connected to the outer cables and the SPA (Fig. 3). This setup enables simultaneous KPFM and current-voltage measurements.

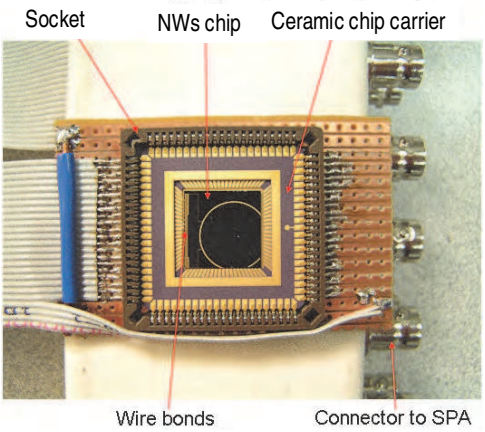

Fig. 3. The custom made electronics connections to the nanowire chip

3. Non-uniform dopant distribution along Si nanowires revealed by Kelvin probe force microscopy and scanning photocurrent microscopy

The future of semiconductor nanowires as building blocks for high-performance nanoscale devices is promising. However, it remains an important challenge to synthesize materials with sufficient control over composition and doping to compete with existing commercial devices. For example, the performance of existing CMOS technology depends critically on the ability to control the location of dopants to create abrupt homojunctions in Si. Such junctions have been realized in Si nanowires synthesized using the VLS growth mechanism by in-situ doping (Gudiksen, Lauhon et al. 2002; Yang, Barrelet et al. 2006), but unintentional surface doping caused by vapor-solid deposition on the sides of the nanowires during growth can complicate the formation of strictly axial homojunctions. Evidence of surface doping has been seen in phosphorous-doped Ge nanowires by electrical characterization (Tutuc, Chu et al. 2006) and atom probe tomography (Perea, Hernesath et al. 2009), and in boron doped Si nanowires by Raman spectroscopy (Imamura, Kawashima et al. 2008). In each of these cases, the nanowires were highly tapered, which is indicative of significant Vapor-solid deposition during synthesis. Even in the absence of tapering, it was shown (Allen, Perea et al. 2009) through scanning photocurrent microscopy that surface doping can occur for phosphorous-doped Si nanowires, resulting in a nonuniform doping profile.

KPFM and scanning photocurrent microscopy (SPCM) were used to measure the doping distribution along single phosphorous doped silicon nanowire grown by the VLS method. A non-linear potential drop along biased silicon nanowires is detected both by measuring the surface potential directly via KPFM and by integrating the photocurrent measured by SPCM (Allen, Perea et al. 2009). These variations in the potential and field are further analyzed to extract the longitudinal dopant distribution along an individual silicon nanowire. The results show a very good agreement between the two methods to quantitatively detect potential, field and doping variations along doped silicon nanowires. Considering that KPFM measures the surface potential whereas SPCM samples the nanowire volume, the correlation between these two methods can improve our understanding regarding the role of surfaces vs. bulk in nanowires electrical properties.

Since the KPFM measures the surface potential profile, it is used as a "four-point-probe" where the scanning tip replaces the two inner contacts of the conventional setup. Although KPFM measures the potential at the surface, in the case of heavily doped wires used here, this potential can be considered, to a very good approximation, as the bulk nanowire potential. The current through the nanowire is measured and can be used to calculate the local effective doping, $N_D(x)$ along the Si nanowire:

$$j / E(x) = \sigma = q\mu N_D(x) \tag{7}$$

where j is the current density, $E(x)$ is the local electric field, σ is the electrical conductivity, q is the elementary charge and m is the mobility for electrons. $E(x)$ is simply obtained by differentiating the measured surface potential along the nanowires. Figure 4(b) shows the expected potential profile along a biased Si nanowire for the case of uniform doping, in contrast to the case of gradually decreasing doping (Fig. 4(c)). Figure 4(d,e) shows the KPFM-measured surface potential profiles along an *n*-Si nanowire under several applied potentials (-3V to 3V with 1V steps). The voltage was applied by grounding one contact and biasing the other, while the back gate electrode was grounded throughout the whole measurement. The potential peaks are due to the applied bias at the left and the right metal contacts. The black dashed lines represent a linear potential drop and therefore help to visualize the deviation of the measured potential profiles from the case of a uniform doping concentration. The perpendicular doted lines (blue) represent the edges of the metal contacts. When applying the bias to the contact closer to the gold catalyst end, the surface potential profile is concave (Fig. 4(d)), while biasing the other contact the profile is convex (Fig. 4(e)). Nevertheless, the absolute averaged electric field (the average was done for four measurements where the applied bias was 1V and -1V, each time on a different contact; the error represent the standard deviation) is always larger near the gold catalyst (Fig. 5(a)), and therefore such a potential curvature is expected. For this reason, the observed field gradient is due to intrinsic variations within the nanowire itself rather than effects related to the metal electrodes. Furthermore, the field gradient is too small to cause significant variations in the local carrier mobility, so we assume a constant mobility of ~150 $cm^2V^{-1}s^{-1}$ (Ben G.Streetman 1999) consistent with electrons in bulk silicon doped to similar levels. This assumption, together with the measured potential, allows one to extract the longitudinal dopant distribution along the Si nanowire as explained above.

Figure 5(b) shows the averaged doping profile extracted by applying 1V and -1V, each time for a different contact. The doping profile increases monotonically along the 8μm long nanowire. The rate of increase is greater when the PH_3 partial pressure is increased (Allen, Perea et al. 2009). In all cases, the doping is higher further from the catalyst side. This is consistent with the fact that this end of the wire was exposed a longer time to the PH_3 gas.

Next, the potential profiles obtained by the SPCM were used for direct comparison with the KPFM data. Since the SPCM measurements were conducted on two-terminal devices, extraction of the absolute potential profiles from the SPCM-measured photocurrent required knowledge of a proportionality factor, representing the potential drop over the contacts, which can be determined by four-probe measurements (Allen, Perea et al. 2009). Therefore, we have scaled and offset the integrated photocurrent profiles to fit the measured KPFM potential profiles, as the latter represent the actual nanowire potential. The scaling factor was 1.5±0.1 for all curves. Figure 6 shows the normalized integrated-photocurrent profiles measured by the SPCM together with the KPFM measured potential profiles for the same wire under the same applied potentials (1V, -1V for each one of the contacts). The

perpendicular doted lines (blue) represent the edges of the metal contacts. Our results show an excellent agreement between these two methods, and confirm the validity of the potential measurements by the SPCM method.

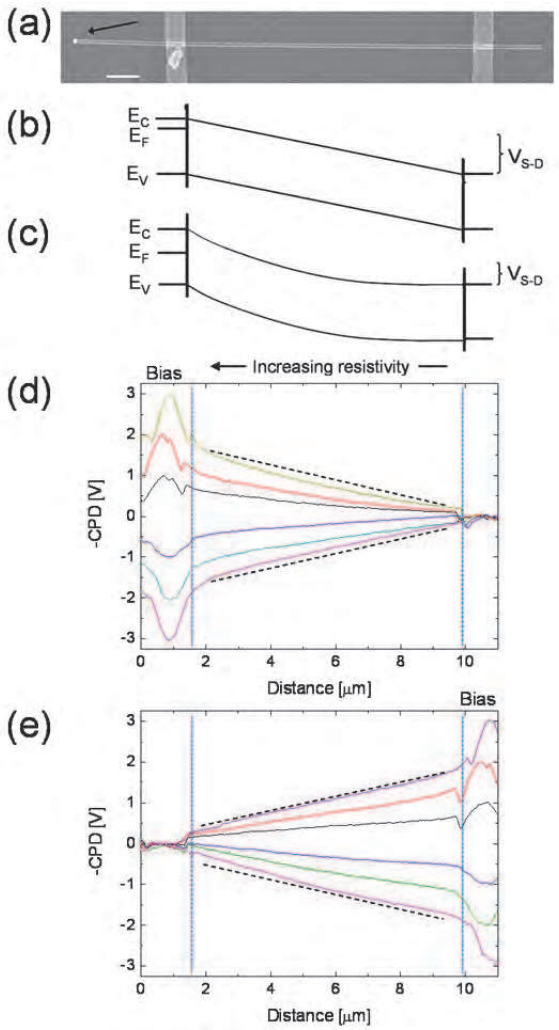

Fig. 4. **(a)** HRSEM image of a typical nanowire device used in our measurements. The Au catalyst is marked by an arrow, contacts are made out of Ni, scale bar is 1μm; schematic band-diagram for the case of a uniformly **(b)** and non-uniformly **(c)** doped Si nanowires under an applied bias. -CPD measured profiles along *n*-Si nanowire biased at different voltages (-3V to 3V with 1V steps), applied to the gold catalyst end **(d),** and to the other side **(e)**. The perpendicular doted lines (blue) represent the edges of the metal contacts. The dashed lines (black) are a guide to the eye to show the deviation from a linear potential profile in the case of a uniform doping distribution.

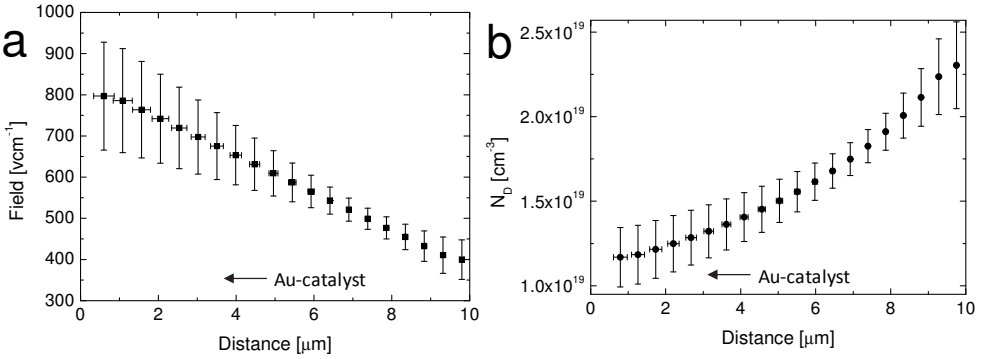

Fig. 5. Averaged electric field **(a)** and doping **(b)** profiles extracted from the measured KPFM profiles along biased *n*-Si nanowire (the average is between four cases where the applied bias was 1V and -1V, each time for a different contact. The error bars represent the standard deviation of the four measurements).

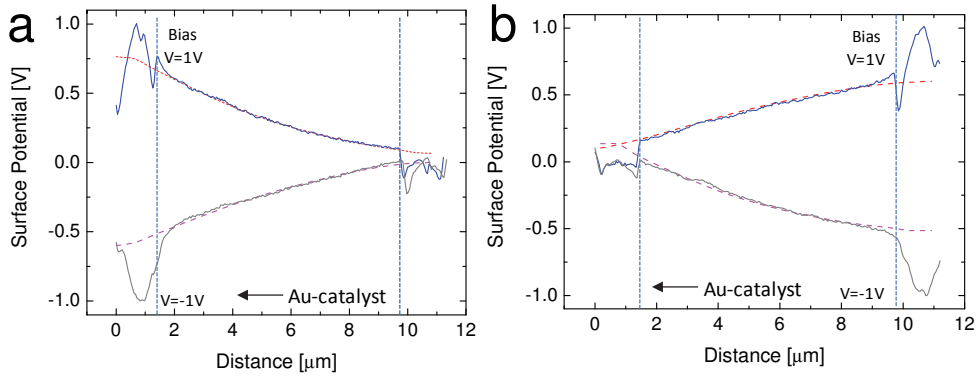

Fig. 6. Surface potential (solid lines) and normalized integrated-photocurrent (dashed lines) profiles along biased *n*-Si nanowire when the bias is applied to the gold catalyst end **(a)** and to the other contact **(b)**. The perpendicular doted lines (blue) represent the edges of the metal contacts.

There are several consequences of the observed non-uniform axial doping. As pointed out by others (Tutuc, Chu et al. 2006; Kempa, Tian et al. 2008), the synthesis of complex axial doping profiles is complicated by unintentional radial doping profiles. Surface doping may also diminish the influence of surface states on conductivity (Kimukin, Islam et al. 2006; Seo, Sharma et al. 2006) by narrowing depletion layers. Even in the absence of surface states, a radially non-uniform doping profile will create a radially non-uniform potential and could produce carrier confinement at or away from the surface. Moreover, considering that KPFM measures the surface potential whereas SPCM the nanowire volume, the excellent

agreement between the two methods and the fact that the surface is more heavily doped leads to the conclusion that most of the current-flow takes place between the outer shell of the nanowire and its core. Measurements of the radial doping profile (presented in the next part) are needed to understand how great is the influence of this surface doping on operating devices.

In summary, we have measured the variations of potential and electric field along biased *n*-Si nanowires by KPFM and SPCM, respectively. The potential profiles indicate a non-uniform doping along VLS based *n*-Si nanowires as recently reported (Allen, Perea et al. 2009). This non-uniformity occurs as a result of the exposure of the nanowire surface to PH_3 gas throughout the growth. In addition we have shown good correlation between KPFM and SPCM to quantitatively detect potential, field and doping variations within doped Si nanowires.

4. Measurement of radial dopant distribution and diffusion in individual Si nanowire

There are very few methods that can be used to measure the dopant concentration and distribution in a single nanowire. Radial dopant profiling in silicon nanowires using capacitance-voltage measurements was recently demonstrated (Garnett, Tseng et al. 2009) where the nanowire doping was controlled by post-growth BCl_3 gas diffusion. They have found that the dopant concentration decreased by almost two orders of magnitude over a radial distance of 25 nanometers from the wire circumference to its center. 3-D atom probe tomography was used (Perea, Hernesath et al. 2009) to directly measure the dopant concentration in individual tapered Ge nanowires. They have found that differences in precursor decomposition rates between the liquid catalyst and the solid nanowire surface result in a radial dopant decrease of one and a half orders of magnitude for a radial distance of 10 nanometers.

Here, we quantitatively demonstrate the important role of dopant diffusion taking place during VLS growth of individual silicon nanowires. We have used KPFM to measure the active radial dopant distribution within a single untapered *n*-type silicon nanowire. It was found that the dopant concentration decreases by almost two orders of magnitude from the wire surface to its core. Moreover the profile is consistent with dopant diffusion during the growth with a diffusion coefficient of D=1x10^{-19} m^{2}s^{-1} which is much larger than the expected value for this temperature in bulk silicon. This implies that P diffusion during the VLS growth of silicon nanowires is very significant and subsequent thermal annealing must be used when a homogenous dopant distribution is required.

Before etching the wires, the active dopant concentration at the nanowire surface was determined to be ~1x10^{20} cm^{-3} by measuring the potential drop along a biased nanowire using KPFM and assuming electron mobility of ~ 150 cm^{2}V^{-1}s^{-1} as described in the previous section.

The method for measuring the radial dopant distribution by KPFM is described schematically in Figure 7(a) in both cross sections and top views. It is based on surface etching of a portion of a contacted nanowire (Allen, Hemesath et al. 2009), followed by measurement of the potential difference between the etched and the unetched areas using KPFM. This process is repeated several times to gradually remove material, and the surface potential difference (between the etched and unetched parts) is measured for a number of nanowire radii. The radial dopant distribution is then obtained by fitting the

measured potentials with a 3D solution of Poisson equation as explained in more details below.

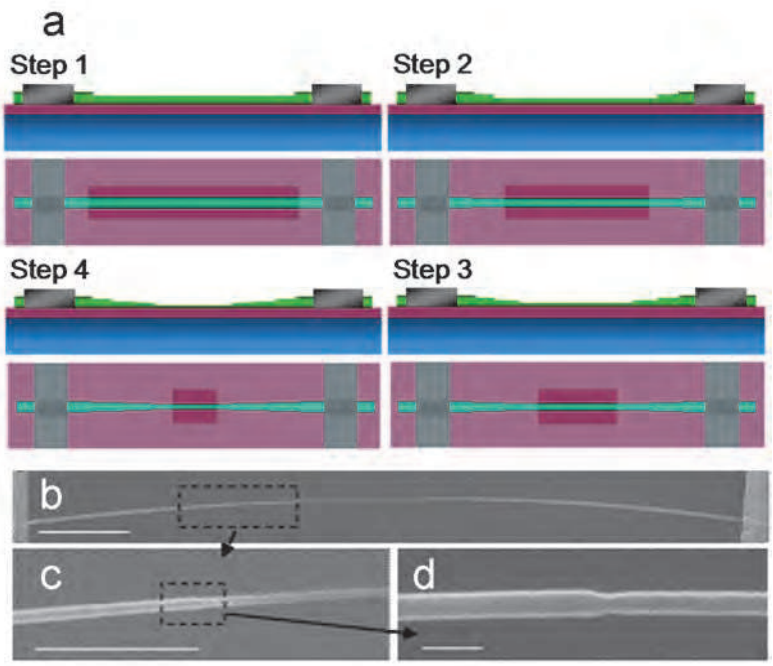

Fig. 7. (a), schematic illustration of four etching steps and their resulting nanowire structures; in each step a different size of window is opened over the nanowire channel by electron-beam lithography and few nm of the nanowire surface are etched. (b), HRSEM image of the nanowire after five etching steps, scale bar is 1μm. (c), magnified HRSEM image showing three steps over the nanowire, scale bar is 1μm. (d), magnified HRSEM image on a single step, scale bar is 100nm.

The nanowire selective etching was carried out by coating the sample with a thick layer of PMMA and defining windows by EBL in the center of the contacted wire device. The PMMA is protecting the metal contacts and ensuring that the nanowire is etched only in the exposed region defined by the window as demonstrated in Figure 7. Wet chemical etching was carried out by the following procedure: After a short oxygen plasma clean, the native oxide was removed using a 2-second buffered HF etch, and a few nanometers (5-7nm) of the silicon surface were subsequently removed by a 20-second NH_4F etch. Four sequential wet chemical etching steps were applied, where in each step a smaller window was defined and opened; the result was a stairs case-like structure of the nanowire, as schematically depicted in Figure 7. An HRSEM image of three etching steps (Fig. 7 (c)) and a magnified image of a single step (Fig. 7(d)) show parts of the etched nanowire. We note that, following each etching step, the nanowire surface becomes rougher resulting in a larger distribution of nanowire diameters; having a larger number of nanowire radii enables the determination of

the radial dopant distribution with a better depth resolution, as explained in the next sections.

Figure 8 shows the measured topography (a), and -CPD (b) of a single silicon nanowire following four etching steps. For convenience we present -CPD, because it expresses the surface potential of the nanowire. The observed change in -CPD as a function of the etching-depth indicates a change in the Fermi level (E_F) relative to the sample local vacuum level (E_{LVL}) as shown in Figure 8 (c). We attribute this change to a decreasing doping level from the nanowire shell to its core. The observed correlation between the topography and -CPD cannot be due to the changes in the scanning tip height as the nanowire is etched. Such tip convolution effects were analyzed by us in the past (Strassburg, Boag et al. 2005) and have shown that such small (<60mV) CPD differences between neighboring areas (in this case the nanowire and the substrate) cannot account for the CPD changes measured here.

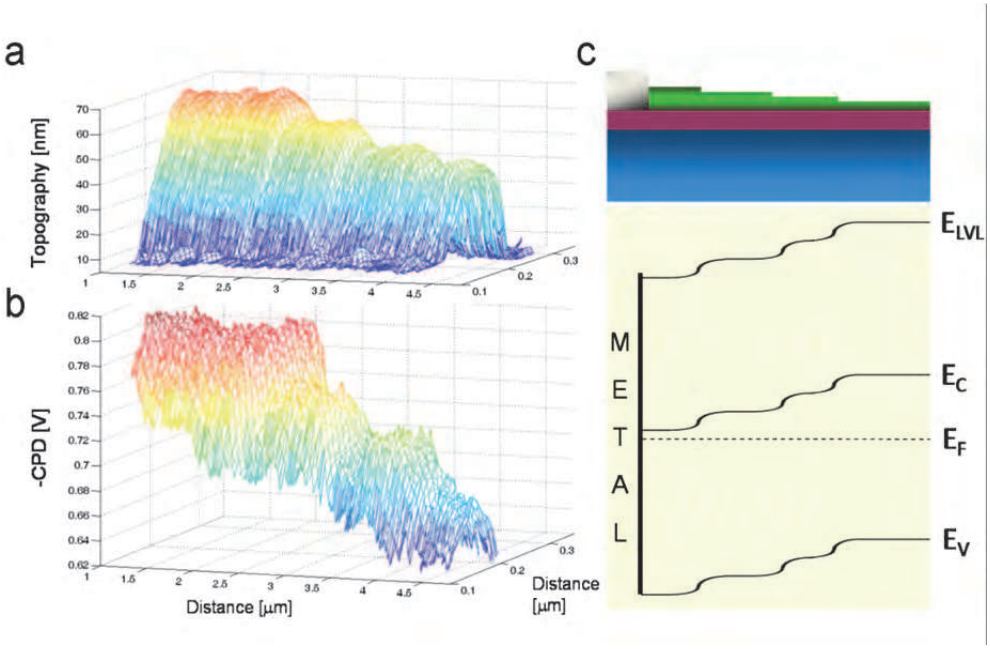

Fig. 8. **(a)**, 3D AFM image showing four steps in topography, each step is ~ 7 nm. **(b)**, 3D -CPD image showing four steps in -CPD, each step is ~ 15 mV. **(c)**, schematic band diagram of the etched silicon nanowire.

To obtain the radial dopant distribution, both the topography and the -CPD values from all the measured points of the top 10 nm etched nanowire area were averaged in order to minimize the effect of the nanowire curvature. Subsequently, a plot of the averaged surface potential as a function of the radial etching distance was obtained (symbols Fig. 9); the measured profile was averaged over three different wires measured at the higher doped side. The solid lines in Figure 9 are surface potential profiles calculated as explained in the following paragraph.

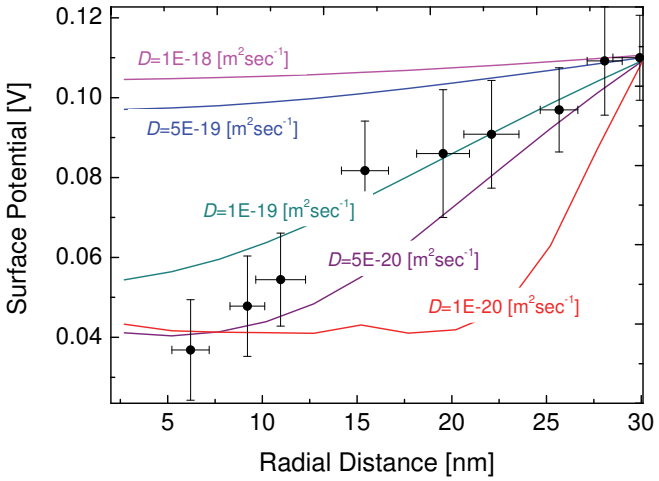

Fig. 9. Simulated (solid lines) and measured (symbols) surface potential profiles. Simulation was carried out for different doping profiles; each profile was calculated for a different diffusion coefficient. The measured surface potential profile was averaged over three different samples; shows a relatively good agreement with the calculated doping profile for $D \sim 1\text{x}10^{-19}$ m^2s^{-1} (until a radial distance of ~12nm). The error bars in the measured profile represent the standard deviation in the KPFM measurement for all the three nanowires.

As mentioned above, during the VLS growth dopants are incorporated into the wire both through the gold catalyst (causing a uniform dopant concentration, $C\ (t=0)$) and through the surface by uncatalyzed decomposition. Given the higher surface doping and the growth temperature of 460°C it is reasonable to assume that the dopant profile is governed by P diffusion into the nanowire. Thus, the time-dependent diffusion equation with cylindrical symmetry was solved to obtain the radial dopant profile of the nanowire (Crank 1975):

$$C(r,t) = k\left(t - \frac{a^2 - r^2}{4D_{Growth}}\right) + \frac{2k}{aD_{Growth}} \sum_{n=1}^{\infty} \exp\left(-D_{Growth}\alpha_n^2 t\right) \frac{J_0(r\alpha_n)}{\alpha_n^3 J_1(a\alpha_n)} + C\big|_{t=0} \qquad (8)$$

The diffusion equation was solved for different diffusion coefficients with a linear increasing concentration of P (with the growth time) on the surface of the nanowire, accounting for the evolving surface doping during the VLS growth. The linear increasing surface doping was determined from the longitudinal dopant distribution along the nanowire and the growth rate of the nanowire; both were assumed to be approximately linear. Thus, a surface doping rate (dC/dt) of ~ $1\text{x}10^{17}$ $cm^{-3}s^{-1}$, was estimated by the product between the growth rate of the nanowires (dZ/dt ~ $1\text{x}10^{-6}$ $cm\ s^{-1}$) and the surface doping distribution along the nanowires ($dC/dZ \sim 1\text{x}10^{23}$ cm^{-4}), where C is the P concentration on the nanowire surface; t is time and Z is the longitudinal distance along the nanowire. The background concentration of P inside the nanowire which was assumed to be homogeneous and caused as a result of intentional doping through the Au catalyst was determined to be $1\text{x}10^{18}cm^{-3}$ in order to be self consistence both with the P surface concentration ($1\text{x}10^{20}$ cm^{-3}) and with the extracted doping profile.

These profiles are then used as an input to the 3D Poisson equation solved using the *Sentaurus TCAD* device simulator *(Synopsys inc.)* to obtain the wire surface potential as a function of the etching height. This solver is a 3D finite element simulator which solves the Poisson equation coupled with the continuity equation for holes and electrons for the desired doping profile. The model follows the real device geometry including the topography steps resulted from the applied etching. Correlation between the radial distance and the surface potential was carried out by taking the potential and height values from the surface of each stair. Figure 9 shows both the simulated and the averaged-measured surface potential profiles. The calculated doping profile for $D = 1x10^{-19}$ m^2s^{-1} (Fig. 10(a)) leads to a surface potential profile which is in agreement with the measured profile up to a radial distance of ~12nm.

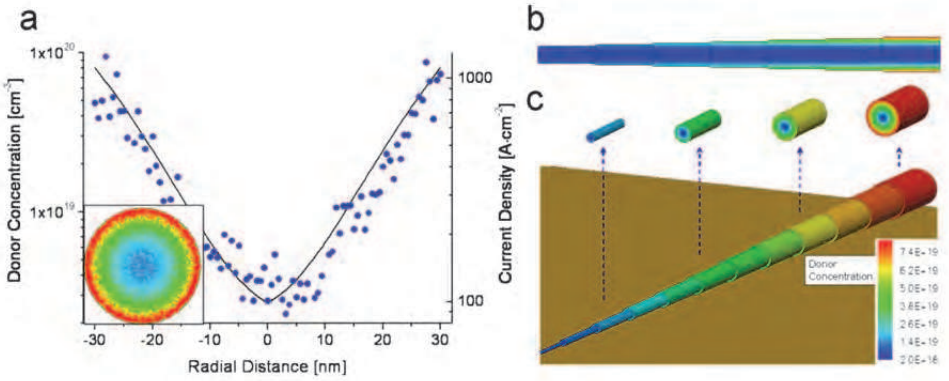

Fig. 10. **(a)**, calculated radial doping profile for $D = 1x10^{-19}$ m^2s^{-1} (solid line) and simulated current density (symbols in the graph and inset image) through the nanowire under an applied bias of 0.1V. P concentration decreases exponentially from ~$1x10^{20}$ cm^{-3} at the nanowire surface to ~$2x10^{18}$ cm^{-3} at the nanowire core. The current density is higher (> order of magnitude) close the nanowire surface in agreement with the doping profile. Calculated 2D **(b)** and 3D **(c)** of the dopants distribution in the nanowire for $D = 1x10^{-19}$ m^2s^{-1} following several etching steps (a matched 3D distribution of the potential was used to extract the radial surface potential profile).

Calculated 2D and 3D of the dopants distribution in the nanowire following several etching steps for $D = 1x10^{-19}$ m^2s^{-1} are presented in Figure 10(b) and 10(c), respectively. These dopant profiles are used for calculating the current density through the nanowire under an applied bias voltage of 0.1V between the two contacts. The resulting non-uniform current flow (symbols and inset image) is shown in Figure 10(a) together with the dopant distribution profile (solid line). The current density is larger by more than an order of magnitude at the nanowire circumference compared to its interior part.

Following etching of more than 15nm, the measured surface potential profile deviates (downward bending) from the calculated dopant diffusion profile indicating a lower Fermi energy with respect to the conduction band minimum, E_c. This deviation can be due to negatively charged surface states which induce upward band bending at the wire circumference. This was simulated by including a negative surface charge

(N_{SC}) of = 5x10^{11} cm^{-2}, which has been estimated for Si nanowires by several groups (Bjork, Schmid et al. 2009; Garnett, Tseng et al. 2009). Figure 11(a) shows the simulated (solid lines) surface potentials for a diffusion constant of D =1x10^{-19} m^{2}s^{-1} including negative surface charge (N_{SC}) of 0, 5x10^{11} and 1x10^{12} cm^{-2} together with the average-measured potential profile (symbols). As the nanowire is etched, with a concurrent decrease in its surface doping concentration, the existence of a negative surface charge results in larger surface band-bending (Fig. 11(b)).

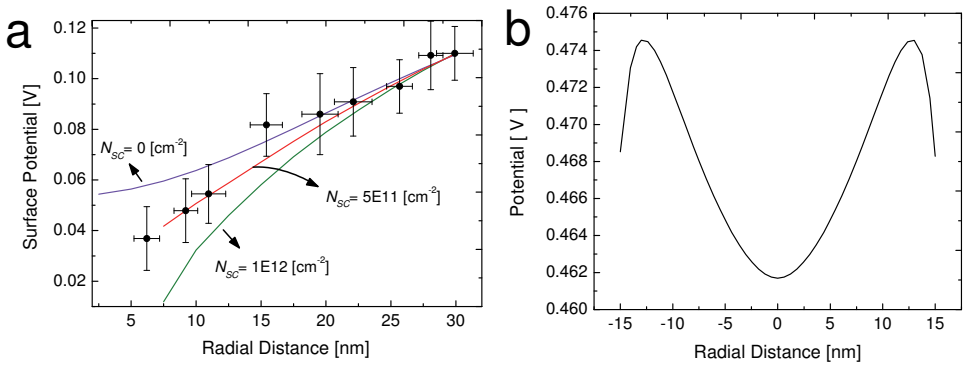

Fig. 11. **(a)** Simulated (solid lines) surface potential profiles with negative surface charge of 0, 5x10^{11} cm^{-2} and 1x10^{12} cm^{-2} and the averaged measured profile (symbols). The error bars in the measured profile represent the standard deviation in the KPFM measurement for all the three nanowires. The averaged measured profile shows a relatively good agreement with the simulated profile for N_{SC} = 5x10^{11} cm^{-2}. **(b)** Simulated surface potential band-bending of the etched nanowire with the presents of negative surface charge of N_{SC} = 5x10^{11} cm^{-2}.

The extracted value for the diffusion coefficient, D~1x10^{-19} m^{2}s^{-1}, is considerably larger from any value extrapolated from high temperature data (F.F.Y.Wang 1981), and to the best of our knowledge there are no reports of P diffusion in bulk silicon with conditions resembling the VLS growth. However, many works have shown that P diffusion is remarkably enhanced under several conditions. For example, the diffusion is enhanced when the surface concentration of P exceeds a value of n_s ~1x10^{20} cm^{-3} (Matsumot.S, Yoshida et al. 1974; F.F.Y.Wang 1981; Gorban and Gorodokin 1988) (as in the present study). This high surface concentration leads to an apparent "kink" in the dopant profile which is a result of dissociation of $P^+V^=$ ion pairs, causing an enhanced diffusion in the form of a "tail" (Schwettmann and Kendall 1972). It was shown (Fair and Tsai 1977) that this effect increases the diffusivity at 600^{o}C by four orders of magnitude relative to the value extrapolated from high temperatures; they have also shown that this enhancement will be even larger at lower temperatures. It was reported (Shibayama, Masaki et al. 1976) that Boron and Arsenic diffusivities can reach values of ~ 1x10^{-20} m^{2}s^{-1} in the temperature range of 500-800^{o}C and with no sign for temperature dependence. They associated this enhancement to a generation of excess vacancies at low temperatures. Figure 12 summarizes most of the literature reported data of P low temperature diffusion for the case of high surface concentration in comparison with the our result. The figure shows that the maximum predicted diffusivity, based on the above, for our growth temperature of

460°C is ~ 1x10^{-21} m^{2}s^{-1} (see our linear fit in Fig. 12) which is still smaller than our extracted value. This may be attributed to: a) generation of excess vacancies at the nanowires surface, b) relatively short time and range of the dopants diffusion during growth (10-15 minutes and 30nm, respectively) in nanowires compared to bulk; and c) to the very large surface to volume ratio present in nanowires (Fig. 13d).

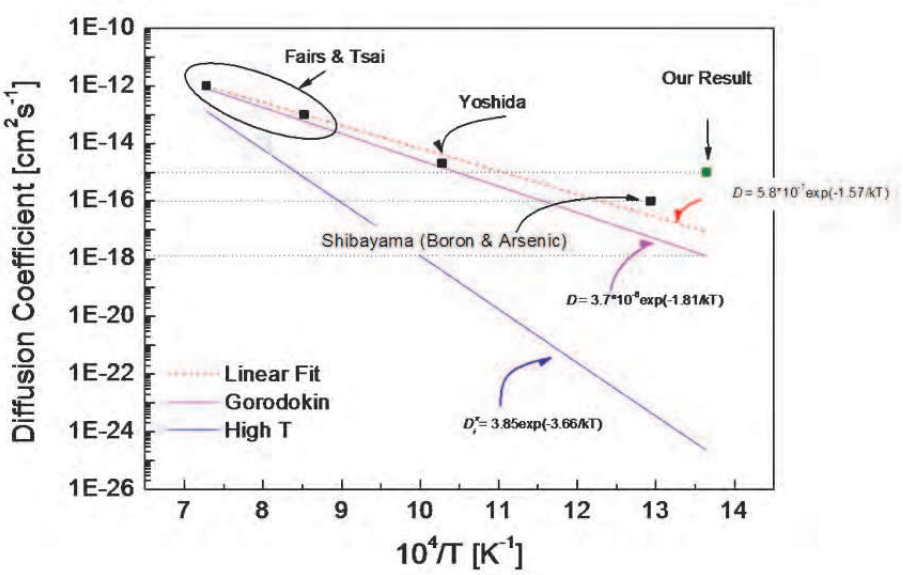

Fig. 12. Summary of the diffusion coefficients from several literature sources including, high surface concentration and low temperature reports together with high temperature data and our result. The red dashed line is a linear fit which made by us in order to predict what should be the diffusivity of P at 460C. It is related to the data from the works of Fair & Tsai, Yoshida, and Shibayama. This linear fit agrees with the following formula: 5.8x10^{-7}exp (-1.57/kT).

Furthermore, the kink observed in our KPFM measured surface potential profiles (see individual wire profiles, Fig. 13) is in agreement with P diffusion in bulk silicon and may imply that similar diffusion mechanisms exist in nanowires (Tsai 1969). However more dopant distribution measurements are required in order to obtain the P diffusion mechanism in silicon nanowires.

In summary, KPFM was used to map the radial active dopant distribution within a single *n*-type silicon nanowire grown by the VLS method. Results show a radial decrease in the dopant concentration from the surface toward the wire core, with a change of almost two orders of magnitude even when there is no indication of taper. Furthermore, the diffusion coefficient of the dopant P atoms in the silicon nanowires was estimated to be D ~1x10^{-19} m^{2}s^{-1}. The latter does confirm the diffusion of P from the vapor phase into the silicon nanowire during its growth, in the VLS method. Finally, the simulated non-uniform current density through the nanowire demonstrates the implications of such non homogenous dopant distribution on the performance of nanowire based electrical devices.

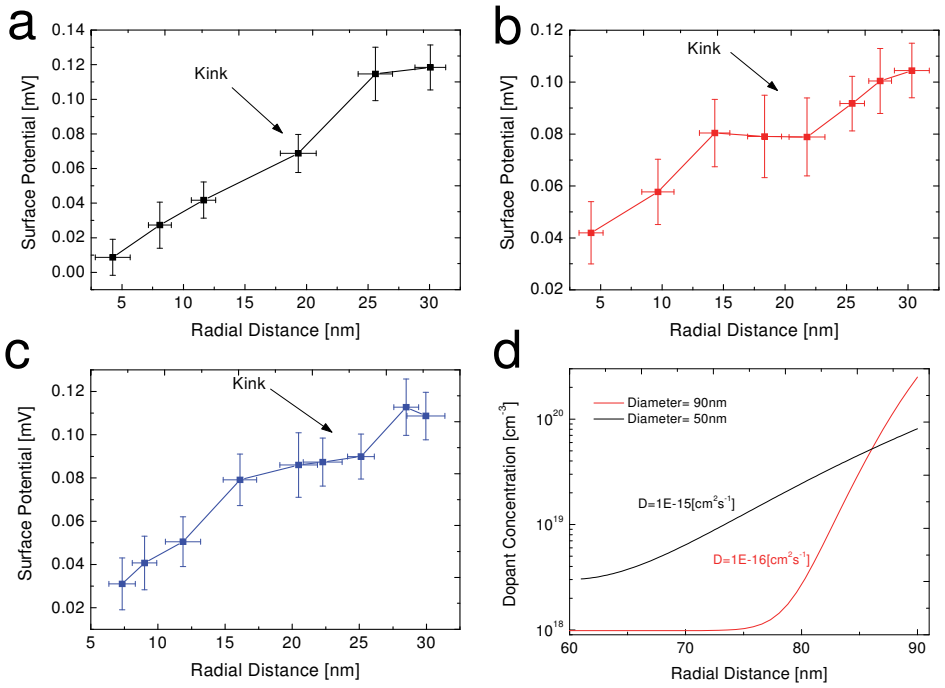

Fig. 13. **(a, b, c)** Individual measured surface potential profiles for three nanowires from the same growth show a kink in the potential profile in a radial distance of ~ 23nm. The same kink has been reported for the case of P diffusion in bulk silicon. The error bars represent the standard deviation in the KPFM measurement. **(d)** Measured radial dopant concentration profiles and diffusivities for nanowires with different diameters, showing higher diffusivity for lower diameter.

5. Obtaining uniform dopant distribution in Si nanowires

As presented in parts 3-4, vapour-solid deposition during nanowire growth can lead to a highly non-uniform distribution of dopants both along the nanowire and across its radii, even in the absence of tapering. In this section, the high diffusivity of P dopants that occurs in nanowires was exploited to reduce the radial non-uniformity by employing thermal annealing following nanowire growth. In addition, no measurable diffusion of the Au catalyst was observed, as probably would occur at higher temperature treatment (Hannon, Kodambaka et al. 2006).

Thermal annealing of the nanowires (prior to their separation from the substrate by sonication i.e. before device fabrication) was carried out at 460 ^{o}C in forming gas (90% N_2 and 10% H_2) for one hour using a commercial *AS-MICRO* system of *ANNEALSYS* Company. The radial dopant distribution for both as-grown and annealed nanowires was measured by etching a section of the nanowire surface, followed by the measurement of the potential difference between the etched and the unetched areas using KPFM (as described in the previous part).

Figure 14a presents the simulated (solid lines) and measured (symbols) surface potential profiles for both as-grown and annealed nanowires. The plotted profiles of measurements are averages from 5 different wires, measured at the end that is more highly doped; the error bars represent the standard deviation in the measurement for all the averaged profiles. The simulated potential profiles in Figure 14a are produced after first calculating the dopant profile. As mentioned earlier, during the VLS growth dopants are incorporated into the wire both through the gold catalyst (causing a uniform dopant concentration, $C\ (t=0)$) and through the surface by uncatalyzed decomposition. The time-dependent diffusion equation (eq. 8) was solved to obtain the radial dopant profile inside the as-grown nanowires. The calculated profile assuming D_{Growth}= 1x10^{-16} cm^{2}s^{-1} (green solid line in Figure 14b) is in good correspondence with the measured surface potential profile (empty symbols in Figure 14a).

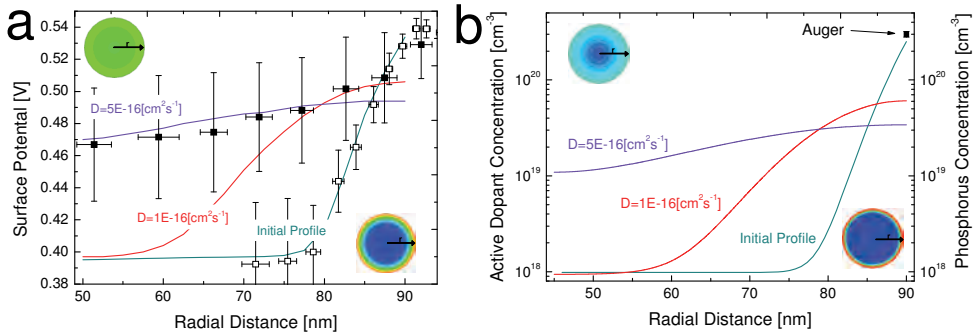

Fig. 14. **(a)** simulated (solid lines) and measured (symbols) radial potential profiles for the as-grown (initial profile) and annealed nanowires. **(b)** calculated radial active dopants concentration profiles (left scale) of the as-grown (initial profile) and annealed nanowires and Auger spectroscopy measurements (right scale) of the nanowire P surface concentration (symbol) before and after the anneal. The insets are the 2D potential **(a)** and concentration **(b)** profiles for the as-grown (right sides) and for the annealed (left sides) nanowires.

The same procedure was used to simulate the radial surface potential profile for the annealed nanowires following a calculation of the dopant diffusion. Thus, we have used the initial dopant distribution, $f(r)$, (established by equation 8 for the as-grown nanowires) to solve the diffusion equation for impermeable cylinder (Crank 1975) (to simulate the annealing treatment):

$$C(r,t)=\frac{2}{a^2}\left\{\int_0^a rf(r)\,dr+\sum_{n=1}^{\infty}\exp\left(-D_{anneal}\alpha_n^2 t\right)\times\frac{J_0(r\alpha_n)}{J_0^2(a\alpha_n)}\int_0^a rf(r)J_0(\alpha_n r)\,dr\right\} \tag{9}$$

Here, C is the dopant concentration, r is the radial distance from the middle of the nanowire, $f(r)$ is the initial dopant distribution, α_n's are the roots of: $J_1(a\alpha_n)=0$, a is the nanowire radius and D_{anneal} is the diffusion coefficient during the annealing. Figure 14a, b present surface potential and dopant concentration profiles, respectively, for two different diffusion coefficients after 1 hour of annealing. Using the calculated profile assuming D_{anneal}= 5x10^{-16} cm^{2}s^{-1} (purple solid line in Figure 14b), we get good agreement with the measured surface potential profile (filled symbols in Figure 14a). The insets in figure 14a, b are the 2D

potential and concentration profiles, respectively, for the as-grown (right side) and for the annealed (left side) nanowires.

We note the relatively constant, high measured surface potential of the nanowires implies that a high surface dopant concentration remained after annealing. In order to explore how the annealing process affected the surface P concentration and the fraction of active dopants, we conducted nano-scale Auger measurements to evaluate the P concentration (for Auger spectroscopy: Si nanowires were deposited onto a GaAs wafer, measured by a PHI 700Xi Scanning Auger nanoprobe). Comparing the Auger transitions of Si and P obtained in locations comparable to where the KPFM measurements were done revealed a similar surface dopant concentration (symbol in Fig. 14b) of 0.51% ±0.03% (or $2.55 \times 10^{20} \pm 0.15 \times 10^{20}$ cm^{-3}, taking the Si solid concentration to be 5×10^{22} cm^{-3}) before and after annealing. The high surface concentration may result not only from direct surface doping, but also from surface segregation of P atoms, which has been predicted to occur in Si nanowires (Fernandez-Serra, Adessi et al. 2006; Peelaers, Partoens et al. 2006) and has been extensively studied in thin films (Nutzel and Abstreiter 1996; Thompson and Jernigan 2007). Specifically, the segregation of P to the Si-SiO interface (Lau, Mader et al. 1989). The stability of this interfacial excess upon annealing, has been observed before in Si thin films (Schwarz, Barton et al. 1981). The high dopant concentration measured in the annealed nanowires is consistent with the expectation of surface segregation.

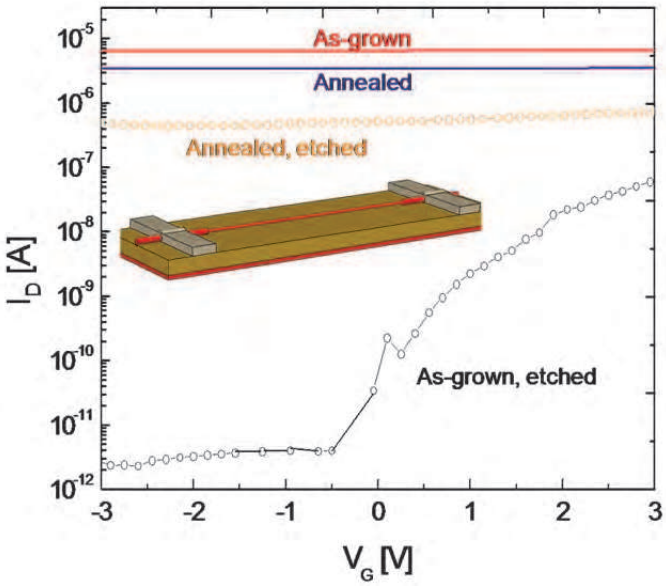

Fig. 15. I_D-V_G current-voltage measurements for as-grown and annealed nanowires before (solid lines) and after (symbols) 20nm etch of the Si surface. The inset is a schematic illustration of the measured etched device.

The redistribution of dopants during annealing was confirmed by current-voltage measurements of two-terminal devices. To highlight the influence of the surface dopants, 20 nm was removed from the surface of both as-grown and annealed nanowires in a single

step, and the characteristics were compared with unetched nanowires (Fig. 15). Etched, as-grown nanowire devices showed rectifying behavior in agreement with previous work (Allen, Perea et al. 2009), and their conductivity was strongly influenced by a back-gate voltage. However, the conductivity of the annealed nanowires was only weakly affected by the back gate voltage both before and after the etching, as expected for higher doped nanowires. This behavior further confirms that the annealing treatment encouraged the diffusion of P atoms from the nanowires surface to core, resulting in a uniform dopant distribution with N_D ~ 1x10^{19} cm^{-3}. Importantly, TEM images show no evidence of Au diffusion after the annealing (Fig. 16c, d), indicating the appropriateness of the low temperature annealing.

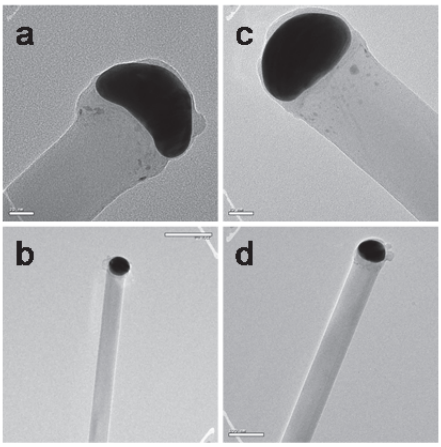

Fig. 16. TEM images of the as-grown **(a, b)** and annealed **(c, d)** nanowires. Scale bars are: 20nm, 200nm, 20nm and 100nm for **(a)**, **(b)**, **(c)**, and **(d)**, respectively.

In summary, a promising approach to obtain uniform radial dopant concentration profiles within P doped silicon nanowires, grown by the VLS process, was demonstrated. In particular, it was shown that low temperature annealing induced the diffusion of P atoms from the enriched nanowire surface to core, with a diffusion coefficient of ~5x10^{-16} cm^{2}s^{-1}, resulting in a more uniform dopant distribution with N_D ~ 1x10^{19} cm^{-3}, and with no sign of Au diffusion into the nanowires or on the surface.

6. Acknowledgment

The authors would like to thank Dr. John Hammond and Dennis Paul from PHI electronics for their help with scanning Auger measurements. This research was generously supported by Grant No. 2008140 from the United States - Israel Binational Science Foundation [BSF].

7. References

Allen, J. E. (2008). Thesis (Ph.D.) "Investigation of carrier transport in semiconductor nanowires by scanning probe techniques." Materials science and engineering department, *Northwestern University*, USA.

Allen, J. E., E. R. Hemesath, et al. (2009). "Scanning Photocurrent Microscopy Analysis of Si Nanowire Field-Effect Transistors Fabricated by Surface Etching of the Channel." *Nano Letters* 9(5): 1903-1908.

Allen, J. E., D. E. Perea, et al. (2009). "Nonuniform Nanowire Doping Profiles Revealed by Quantitative Scanning Photocurrent Microscopy." *Advanced Materials* 21(30): 3067.

Ben G.Streetman, S. Banerjee. (Prentice-Hall, Englewood Cliffs, 1999). "*Solid State Electronic Devices*" 5th ed: 99.

Binnig, G., C. F. Quate, et al. (1986). "Atomic Force Microscope." *Physical Review Letters* 56(9): 930-933.

Bjork, M. T., H. Schmid, et al. (2009). "Donor deactivation in silicon nanostructures." *Nature Nanotechnology* 4(2): 103-107.

Castell, M. R., D. A. Muller, et al. (2003). "Dopant mapping for the nanotechnology age." *Nature Materials* 2(3): 129-131.

Crank, J. (1975). "*The Mathematics of Diffusion*", 2nd ed.; Oxford Univ. Press: Oxford, 1975; p. 75.

Cui, Y. and C. M. Lieber (2001). "Functional nanoscale electronic devices assembled using silicon nanowire building blocks." *Science* 291(5505): 851-853.

Erwin, S. C., L. J. Zu, et al. (2005). "Doping semiconductor nanocrystals." *Nature* 436(7047): 91-94.

F.F.Y.Wang (1981). "*Materials Processing Theory and Practices*"; North Holland: Amsterdam, New York, Oxford, 1981; Vol. 2, p 342.

Fair, R. B. and J. C. C. Tsai (1977). "A Quantitative Model for the Diffusion of Phosphorus in Silicon and the Emitter Dip Effect." *Journal of the Electrochemical Society* 124(7): 1107-1118.

Fernandez-Serra, M. V., C. Adessi, et al. (2006). "Surface segregation and backscattering in doped silicon nanowires." *Physical Review Letters* 96(16).

Garnett, E. C., Y. C. Tseng, et al. (2009). "Dopant profiling and surface analysis of silicon nanowires using capacitance-voltage measurements." *Nature Nanotechnology* 4(5): 311-314.

Gorban, A. N. and V. A. Gorodokin (1988). "Low-Temperature Diffusion of Phosphorus in Silicon." *Russian Physics Journal* 31(9): 56-60.

Grimmeiss, H. G. (1977). "Deep Level Impurities in Semiconductors." *Annual Review of Materials Science* 7: 341-376.

Gudiksen, M. S., L. J. Lauhon, et al. (2002). "Growth of nanowire superlattice structures for nanoscale photonics and electronics." *Nature* 415(6872): 617-620.

Hannon, J. B., S. Kodambaka, et al. (2006). "The influence of the surface migration of gold on the growth of silicon nanowires." *Nature* 440(7080): 69-71.

Haraguchi, K., T. Katsuyama, et al. (1992). "Gaas P-N-Junction Formed in Quantum Wire Crystals." *Applied Physics Letters* 60(6): 745-747.

Imamura, G., T. Kawashima, et al. (2008). "Distribution of active impurities in single silicon nanowires." *Nano Letters* 8(9): 2620-2624.

Kempa, T. J., B. Tian, et al. (2008). "Single and Tandem Axial p-i-n Nanowire Photovoltaic Devices." *Nano Letters* 8(10): 3456-3460.

Kimukin, I., M. S. Islam, et al. (2006). "Surface depletion thickness of p-doped silicon nanowires grown using metal-catalysed chemical vapour deposition." *Nanotechnology* 17(11): S240-S245.

Koren, E., Rosenwaks, Y., et al. (2009). "Nonuniform doping distribution along silicon nanowires measured by Kelvin probe force microscopy and scanning photocurrent microscopy." *Applied Physics Letters* 95(9): 092105.

Koren, E., Berkovitch, N., et al. (2010). "Measurement of Active Dopant Distribution and Diffusion in Individual Silicon Nanowires." *Nano Letters* 10(4): 1163–1167.

Koren, E., Hyun, J. K., et al. (2011). " Obtaining Uniform Dopant Distributions in VLS-Grown Si Nanowires." *Nano Letters* 11(1): 183–187.

Lau, F., L. Mader, et al. (1989). "A Model for Phosphorus Segregation at the Silicon Silicon Dioxide Interface." *Applied Physics a-Materials Science & Processing* 49(6): 671-675.

Martin, Y., D. W. Abraham, et al. (1988). "High-resolution capacitance measurement and potentiometry by force microscopy." *Applied Physics Letters* 52(13): 1103-1105.

Matsumot.S, M. Yoshida, et al. (1974). "Confirmation of Surface Effect Upon Phosphorus Diffusion into Silicon." *Japanese Journal of Applied Physics* 13(11): 1899-1900.

Nutzel, J. F. and G. Abstreiter (1996). "Segregation and diffusion on semiconductor surfaces." *Physical Review B* 53(20): 13551-13558.

Patolsky, F., G. F. Zheng, et al. (2006). "Nanowire-based biosensors." *Analytical Chemistry* 78(13): 4260-4269.

Peelaers, H., B. Partoens, et al. (2006). "Formation and segregation energies of B and P doped and BP codoped silicon nanowires." *Nano Letters* 6(12): 2781-2784.

Perea, D. E., E. R. Hernesath, et al. (2009). "Direct measurement of dopant distribution in an individual vapour-liquid-solid nanowire." *Nature Nanotechnology* 4(5): 315-319.

Perea, D. E., E. Wijaya, et al. (2008). "Tomographic analysis of dilute impurities in semiconductor nanostructures." *Journal of Solid State Chemistry* 181(7): 1642-1649.

Queisser, H. J. (1978). "Recombination at Deep Traps." *Solid-State Electronics* 21(11-1): 1495-1503.

Schwarz, S. A., R. W. Barton, et al. (1981). "Studies of Phosphorus Pile-up at the Si-Sio2 Interface Using Auger Sputter Profiling." *Journal of the Electrochemical Society* 128(5): 1101-1106.

Schwettmann, F. N. and D. L. Kendall (1972). "On the nature of the kink in the carrier profile for phosphorus-diffused layers in silicon." *Applied Physics Letters* 21(1): 2-4.

Seo, K. I., S. Sharma, et al. (2006). "Surface charge density of unpassivated and passivated metal-catalyzed silicon nanowires." *Electrochemical and Solid State Letters* 9(3): G69-G72.

Shibayama, H., H. Masaki, et al. (1976). "Emitter Dip Effect by Low-Temperature Heat-Treatment of Arsenic-Diffused Layer." *Journal of the Electrochemical Society* 123(5): 742-747.

Strassburg, E., A. Boag, et al. (2005). "Reconstruction of electrostatic force microscopy images." *Review of Scientific Instruments* 76(8).

Thompson, P. E. and G. G. Jernigan (2007). "Determination of the surface segregation ratio of P in Si(100) during solid-source molecular beam epitaxial growth." *Semiconductor Science and Technology* 22(1): S80-S83.

Tsai, J. C. C. (1969). "Shallow phosphorus diffusion profiles in silicon." *Proceedings of the IEEE* 57(9): 1499-1506.

Tutuc, E., J. O. Chu, et al. (2006). "Doping of germanium nanowires grown in presence of PH[sub 3]." *Applied Physics Letters* 89(26): 263101.

Wagner, R. S. and W. C. Ellis (1964). "Vapor-liquid-solid mechanism of single crystal growth." *Applied Physics Letters* 4(5): 89-90.

Wang, J. F., M. S. Gudiksen, et al. (2001). "Highly polarized photoluminescence and photodetection from single indium phosphide nanowires." *Science* 293(5534): 1455.

Wang, Y. F., K. K. Lew, et al. (2005). "Use of phosphine as an n-type dopant source for vapor-liquid-solid growth of silicon nanowires." *Nano Letters* 5(11): 2139-2143.

Weaver, J. M. R. and D. W. Abraham (1991). "High-Resolution Atomic Force Microscopy Potentiometry." *Journal of Vacuum Science & Technology B* 9(3): 1559-1561.

Yang, C., C. J. Barrelet, et al. (2006). "Single p-type/intrinsic/n-type silicon nanowires as nanoscale avalanche photodetectors." *Nano Letters* 6(12): 2929-2934.

Nanowires - Implementations and Applications

Edited by Dr. Abbass Hashim

ISBN 978-953-307-318-7
Hard cover, 538 pages
Publisher InTech
Published online 18, July, 2011
Published in print edition July, 2011

This potentially unique work offers various approaches on the implementation of nanowires. As it is widely known, nanotechnology presents the control of matter at the nanoscale and nanodimensions within few nanometers, whereas this exclusive phenomenon enables us to determine novel applications. This book presents an overview of recent and current nanowire application and implementation research worldwide. We examine methods of nanowire synthesis, types of materials used, and applications associated with nanowire research. Wide surveys of global activities in nanowire research are presented, as well.

How to reference

In order to correctly reference this scholarly work, feel free to copy and paste the following:

Elad Koren, Jonathan E. Allen, Uri Givan, Noel Berkovitch, Eric R. Hemesath, Lincoln J. Lauhon and Yossi Rosenwaks (2011). Nano-Scale Measurements of Dopants and Electronic Impurities in Individual Silicon Nanowires Using Kelvin Probe Force Microscopy, Nanowires - Implementations and Applications, Dr. Abbass Hashim (Ed.), ISBN: 978-953-307-318-7, InTech, Available from: http://www.intechopen.com/books/nanowires-implementations-and-applications/nano-scale-measurements-of-dopants-and-electronic-impurities-in-individual-silicon-nanowires-using-k

INTECH
open science | open minds

InTech Europe
University Campus STeP Ri
Slavka Krautzeka 83/A
51000 Rijeka, Croatia
Phone: +385 (51) 770 447
Fax: +385 (51) 686 166
www.intechopen.com

InTech China
Unit 405, Office Block, Hotel Equatorial Shanghai
No.65, Yan An Road (West), Shanghai, 200040, China
中国上海市延安西路65号上海国际贵都大饭店办公楼405单元
Phone: +86-21-62489820
Fax: +86-21-62489821